Journal of Instrumentation

# Detector rates for the Small Angle Neutron Scattering instruments at the European Spallation Source

To cite this article: K. Kanaki *et al* 2018 *JINST* **13** P07016

Published by IOP Publishing for Sissa Medialab

Received: *June 1, 2018*
Accepted: *July 10, 2018*
Published: *July 20, 2018*

# Detector rates for the Small Angle Neutron Scattering instruments at the European Spallation Source

**K. Kanaki,**[a,1] **M. Klausz,**[a,b,c] **T. Kittelmann,**[a] **G. Albani,**[d] **E. Perelli Cippo,**[e] **A. Jackson,**[a,f] **S. Jaksch,**[g] **T. Nielsen,**[h] **P. Zagyvai**[b,c] **and R. Hall-Wilton**[a,i]

[a]*European Spallation Source ESS ERIC, SE-22100 Lund, Sweden*
[b]*Hungarian Academy of Sciences, Centre for Energy Research, 1525 Budapest 114, Hungary*
[c]*Budapest University of Technology and Economics, Institute of Nuclear Techniques,*
*1111 Budapest, Műegyetem rakpart 9, Hungary*
[d]*Dipartimento di Fisica "G. Occhialini", Università degli Studi di Milano-Bicocca, Milan 20125, Italy*
[e]*Istituto di Fisica del Plasma "P. Caldirola", Associazione EURATOM-ENEA/CNR, Milan 20125, Italy*
[f]*Physical Chemistry, Lund University, SE-221 00, Lund, Sweden*
[g]*Forschungzentrum Jülich GmbH, Jülich Centre for Neutron Science JCNS at Heinz Maier-Leibnitz Zentrum,*
*D-85747 Garching, Germany*
[h]*Data Management and Software Centre (DMSC), European Spallation Source ERIC,*
*2200 Copenhagen N, Denmark*
[i]*Mid-Sweden University, SE-85170 Sundsvall, Sweden*

*E-mail:* `Kalliopi.Kanaki@esss.se`

2018 JINST 13 P07016

Abstract: Building the European Spallation Source (ESS), the most powerful neutron source in the world, requires significant technological advances at most fronts of instrument component design. Detectors are not an exception. The existing implementations at current neutron scattering facilities are at their performance limits and sometimes barely cover the scientific needs. At full operation the ESS will yield unprecedented neutron brilliance. This means that one of the most challenging aspects for the new detector designs is the increased rate capability and in particular the peak instantaneous rate capability, i.e. the number of neutrons hitting the detector per channel, pixel or cm$^2$ at the peak of the neutron pulse. This paper focuses on estimating the incident and detection rates that are anticipated for the Small Angle Neutron Scattering (SANS) instruments planned for ESS. Various approaches are applied and the results thereof are presented.

Keywords: Neutron detectors (cold, thermal, fast neutrons); Detector design and construction technologies and materials; Simulation methods and programs; Detector modelling and simulations I (interaction of radiation with matter, interaction of photons with matter, interaction of hadrons with matter, etc)

ArXiv ePrint: 1805.12334

---

[1] Corresponding author.

https://doi.org/10.1088/1748-0221/13/07/P07016

## Contents

## 1 Introduction

The European Spallation Source [1, 2] aspires to become the most powerful neutron source in the world, presenting new challenges for the detector technologies to be used. Fifteen neutron instruments that have been approved as part of the ESS instrument suite are already challenging the traditional detection technologies of the neutron scattering field because of the unprecedented instantaneous counting rates, as well as the requirements for high spatial resolution [3].

LoKI [4, 5] and SKADI [6, 7] are the two Small Angle Neutron Scattering (SANS) instruments endorsed for construction at ESS. LoKI is designed to be a broad-band high intensity instrument with wide polar angle coverage. SKADI offers a broad range of neutron energies as well, in addition to neutron polarisation but with a smaller angular coverage, with its detectors placed at a larger distance from the sample compared to LoKI.

In order to design detectors with the appropriate rate capability and prevent performance compromises on this front, a detailed analysis of the instrument requirements and how they translate to detector requirements is vital. It is also important that such an evaluation be performed with different and complementary approaches, so as to ensure the reliability of the result within acceptable limits.

2018 JINST 13 P07016

The methods used in this paper aim at acquiring a good understanding of the rates LoKI and SKADI are going to achieve by looking at how the scattered neutrons on the sample are distributed in space and time. A realistic worst-case scenario is reproduced, based on which the detector requirements for rate capability are extracted and the choice of detector technology is discussed.

In the following sections the tools and methods used are elaborated upon. The main focus of this evaluation concerns the neutron scattering taking place within the forward solid angle after the sample, as this happens to be the primary area of interest for the SANS technique. This translates to a typical 1 m × 1 m detector area considered for the rate estimates of the scattering characterisation system (SCS). Various detector technologies are explored and their traits are discussed with respect to the instrument rate requirements, as well as the data acquisition (DAQ) design. Last but not least, a smaller area detector acting as a transmission monitor is placed in the path of the direct beam and the same analysis is repeated.

## 2 The rate challenge for the ESS SANS detectors

SANS is one of the most widely used experimental techniques for the investigation of soft matter properties [8]. It uses neutrons that are elastically scattered on the sample at small scattering angles to infer the characteristic length scales of the structures present in it. The scale of the structures of interest that SANS can access is 1–100 nm. Its use of contrast variation from deuterated samples makes it a very powerful tool especially for studies of biological and pharmaceutical interest.

The popularity of the SANS technique makes it a ubiquitous tool at every neutron scattering facility, usually with multiple instruments, targeting both at high availability for the scientific community, as well as satisfying complementary scientific requirements. For the same reason, two SANS instruments have been endorsed at ESS and are currently undergoing different stages of design.

### 2.1 The LoKI instrument

LoKI (the Low-K Instrument) is a wide simultaneous Q range SANS instrument designed primarily with the needs of the soft matter, biophysics and materials science communities in mind. The trend in all of these fields is towards complexity and heterogeneity. Multi-component systems need to be studied as a function of multiple environmental conditions with different structures occurring at different length scales. Small gauge volumes are important to study both intrinsically small samples and for performing scans of heterogeneous samples. There is a need to study systems under the sort of non-equilibrium conditions, such as shear fields, found in real world applications. The ESS flux will enable more routine access of these conditions and also permit fast kinetic studies on a wider range of samples than is possible today. These scientific requirements motivate the requirements that the detector system have a large angular coverage, have good spatial resolution, and have a high rate capability.

### 2.2 The SKADI instrument

The Small-K Advanced DIffractometer SKADI is a high-resolution SANS instrument at the ESS. The scientific areas targeted by SKADI include investigations of smart materials, biological and medical research, magnetic materials and materials for energy storage as well as experiments on

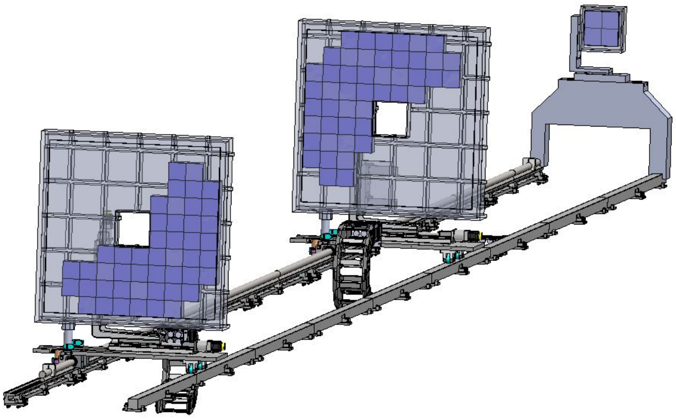

**Figure 1.** Arrangement of three SoNDe detector banks for the SKADI instrument. The single modules for the active area are indicated.

nano-materials and nano-composites. As an additional feature SKADI offers a modular sample environment (3 m × 3 m) that allows custom sample environments, especially for in-situ and in-operando investigations. Those will greatly benefit from the higher flux at the ESS due to lower accessible time scales. In order to make full use of the higher flux, a high-rate capable detector, such as the Solid-state Neutron Detector (SoNDe), is necessary.

The detector setup includes three detector banks at different positions (see figure 1). One detector of 20 cm × 20 cm will be installed at a fixed position 20 m from the sample. The central detector is a 1 m × 1 m with a central 20 cm × 20 cm aperture that will always be at the collimation distance to allow for ideal mapping of resolution between aperture and detector. An identical detector is placed at 1/5 of the middle detector distance from the sample to allow collecting data from higher scattering angles. This setup allows covering three orders of magnitude in the Q-space (reciprocal momentum transfer in the neutron interaction [9], p. 26) in a single shot experiment to enable the observation of fast sample transitions.

### 2.3 Instrument configurations

The chopper settings, collimation length and aperture sizes of a SANS instrument are experimentally configured depending on the sample and the type of measurement to be performed. For the rate estimates a few configurations are selected, aiming at maximising the neutron flux on the sample, in combination with a sample that strongly scatters within the forward solid angle.

The instrument and sample settings used for the rate estimates are listed in table 1. The chopper settings are reflected in the wavelength range, i.e. the $\lambda_{\text{min}}$ and $\lambda_{\text{max}}$ values allowed to reach the sample from the source. The same sample model is used for all instrument configurations. It is a diblock copolymer with a 4.84% scattering probability, an adequate choice for the study of the rear detector geometry. The sample size of 1 cm × 1 cm matches that of the sample aperture. In SANS it is typical to match the collimation length to the sample-detector distance, in order to optimise the resolution capability of the instrument. For the current study though, this distance is fixed at 5 m to get a cross comparison among the detector options presented in the following sections.

**Table 1.** LoKI instrument configurations for the evaluation of rates. The same sample is used for all scenarios. The divergence represents the direct beam size on the detector and is defined by the collimation settings.

| config | collimation length (m) | $\lambda_{\min}$ (Å) | $\lambda_{\max}$ (Å) | source aperture (cm × cm) | sample aperture (cm × cm) | flux on sample (n/cm$^2$/s) | divergence (cm) |
|---|---|---|---|---|---|---|---|
| 1 | 3 | 3.0 | 11.5 | $3 \times 3$ | $1 \times 1$ | $1.00 \times 10^9$ | 8.4 |
| 2 | 5 | 3.0 | 11.5 | $2 \times 2$ | $1 \times 1$ | $2.02 \times 10^8$ | 4.4 |
| 3 | 8 | 3.0 | 10.0 | $2 \times 2$ | $1 \times 1$ | $8.24 \times 10^7$ | 3.0 |

The contributions to the number of neutrons reaching the detector can be broken down to the coherent and incoherent scattering components from the sample, the incoherent scattering from the solvent and the transmitted neutrons, as in eq. 2.1.

$$N = \mathrm{coh}_{\mathrm{sample}} + \mathrm{incoh}_{\mathrm{sample}} + \mathrm{incoh}_{\mathrm{solvent}} + \mathrm{transmission}. \tag{2.1}$$

In the current study, only the coherent scattering from the sample is taken into account, i.e. the actual signal the SANS technique is after. This provides a lower limit to the rate estimates for the SCS. The transmission neutrons are studied separately to shed light on the requirements of the direct beam detector. In the latter case the derived rates serve as an upper limit.

### 2.4 Rate definitions and analytical estimates

The rate definitions used in this study are listed in [10] (page 14) as follows:

- **Global time-averaged incident/detection rate**: the number of neutrons per second entering/recorded by the entire detector.
- **Local time-averaged incident/detection rate**: the number of neutrons per second entering/recorded in a detector pixel, channel or unit.
- **Global peak incident/detection rate**: the highest instantaneous neutron incident/detection rate on the whole detector.
- **Local peak incident/detection rate**: the highest instantaneous neutron incident/detection rate on the brightest detector pixel, channel or unit.

Knowing the scattering fraction F(%) for a SANS sample model, it is possible to get an approximate analytical estimate for the time-averaged incident rates the rear detector is exposed to. The largest portion of the signal-related scattered neutrons is contained within the forward cone subtended by the rear detector, which usually has a polar angle coverage of up to a few degrees, depending on its distance from the sample. As SANS deals with different degrees of freedom compared to other neutron techniques, the neutrons scattered at small angles represent long range correlations and carry information about large distances in real space. The diblock copolymer model mentioned before has a scattering fraction of about 4.8%. For instrument configuration 1 this translates to an upper limit of a global incident time-averaged signal rate of 4.8% $\times\, 10^9$n/s/cm$^2$ flux $\times$ 1 cm$^2$ sample size $=$

$4.8 \times 10^7$ n/s = 48 MHz. The incoherent contribution from the sample and the solvent have to be estimated in addition. If 10% of the incident beam is incoherently scattered in $4\pi$, then the incident fraction within the solid angle subtended by the rear detector is 10% $\times 10^9$ n/s/cm$^2$ flux $\times$ 1 cm$^2$ sample size $\times$ 0.04 sr = 4 MHz. A global time-averaged rate of 52 MHz is to be expected as an upper incident rate limit for the high flux instrument configuration on the rear detector.

### 2.5 The Monte Carlo approach

Analytical rate estimates are based on several approximations and lack the more detailed picture that a Monte Carlo (MC) approach can provide. One fundamental MC tool that is broadly used for instrument design is McStas [11, 12]. It can model all major components of an instrument by sampling an external neutron source distribution and then propagating neutrons through guides, choppers, monochromators, collimators etc. until the sample and beyond. A collection of sample components is also available allowing the neutrons to scatter based on underlying physics models and then be histogrammed by monitor components that act like "detectors". The latter process is of particular interest for the detector design, as it allows the visualisation of the neutrons entering the detector geometry accessing at the same time their full list of properties, e.g. wavelength ($\lambda$), time-of-flight (TOF), position, scattering angle ($\theta$) and optionally user-defined flags. These properties are necessary to differentially study the picture of the impinging neutrons on the detector as a function of time (within a neutron pulse), wavelength and polar angle.

Both ESS SANS instruments are modeled in McStas as part of the design progression. In this paper, a baseline LoKI model is used assuming that no major modifications are anticipated or that future modifications will not impact the predicted rates in a way that completely resets the detector design effort. The deduced rate numbers correspond to the butterfly moderator source ("ESS_butterfly") [13] with a pulse length of 2.86 ms and reflect the maximum accelerator power of 5 MW.

### 2.6 Rate derivation method

As the neutron scattering community is transitioning from the traditional $^3$He detectors to solid converter detectors and more exotic geometries, it becomes important to examine incident and detection rates for all the detector technologies presently evaluated. These scenarios include $^3$He tubes, Boron Coated Straws (BCS) by Proportional Technologies, Inc., the SoNDe detector and the BAND-GEM detector (refs. in respective sections). This practically translates to a variety of channel and pixel geometries, from the familiar two-channel tube read out in charge division mode, to two-dimensional (2D) pixels of rectangular or trapezoidal shape with individual channel readout.

The output of the McStas (2.4.1) simulation that is recorded immediately after the sample is used as input for a subsequent Geant4 [14–16] detector simulation. The latter is performed with the ESS Detector Group Simulation Framework [17]. The file format facilitating this communication is the Monte Carlo Particle Lists (MCPL) format [18, 19]. With the combination of the two software packages it is possible on one hand to take into account the correlations of neutron properties, like TOF, energy, spatial and momentum vectors, and on the other hand to reliably evaluate the detector performance. The Geant4 validation of the latter is addressed elsewhere [20] and is not discussed in this study.

At a pulsed source the peak rate could be more than an order of magnitude higher than the time-averaged one. It is thus important for the qualification of a detector technology for a specific

2018 JINST 13 P07016

application and impacts the readout electronics design. The peak rates also dictate the system design for data collection, aggregation and transfer but as the data are propagated further down the process chain, it is the time-averaged rates that become more relevant for data transfer and storage choices.

Another distinction in the current work is between incident and detection rate. The first would be the upper limit the detector would count, if it had a detection efficiency of 100%. As the detectors have efficiencies that depend on the neutron energy, the instance when the number of incident neutrons is highest is not necessarily the instance of the highest number of detected neutrons. A detector might be illuminated with a high flux but if it is not efficient at the respective neutron wavelengths, there is no concern for saturation. The peak incident rate and peak detection rate do not have to occur simultaneously.

The incident neutrons arrive at the detector with various TOF and energy values. As Geant4 continues to count time for the particles it propagates, the TOF distribution will vary as a function of detector depth. This effect needs to be taken into account for the estimate of the instantaneous peak detection rates for those detectors that record depth information [20–23].

For the derivation of the incident rates, the incident neutron TOF distribution at 5 m after the sample is used, as depicted in figure 2, in order to select the TOF region which contains the highest number of neutrons. Similarly, the maximum of the TOF distribution of detected neutrons is used for the estimate of the highest detection rate.

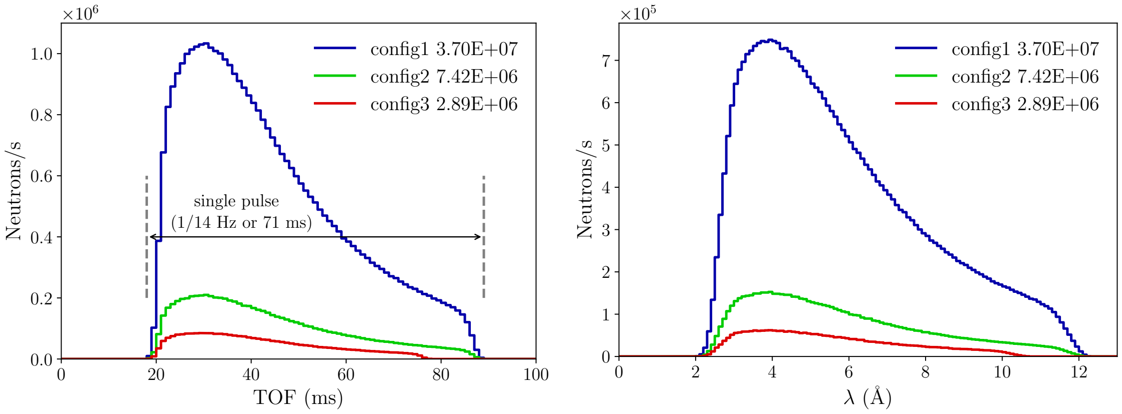

**Figure 2.** A typical neutron TOF and $\lambda$ distribution 5 m after the sample for the three instrument configurations. The global incident rates per configuration appear in the legend in Hz for a standard 1 m × 1 m detector.

The peak number of neutrons can be represented in various ways, e.g. per tube or pixel. When filling the histograms representing the peak rates, the weight of every bin is normalised with the accelerator frequency (14 Hz).

## 3 Tackling the ESS flux with tube geometries

One of the options the neutron scattering community has primarily relied on is $^3$He tube detectors arranged in a single layer, typically with an 8 mm outer diameter and charge division readout. To satisfy the high rate requirements the tubes can be arranged in successive layers of possibly lower detection efficiency, $^3$He or other technology, in order to distribute the detection events in a larger volume and reduce event pile-up. The same can be achieved by reducing the tube size but the increase of dead area compromises the data quality.

### 3.1 Rates for the $^3$He tubes

The Geant4 geometry model implemented for the $^3$He tube (see figure 3) constitutes a typical detector arrangement for many SANS instruments around the world [24–27]. The outer tube diameter is 8 mm with a 0.4 mm wall thickness, a length of 1 m and a total gas pressure of 10 bar with a $^3$He/CF$_4$ mixture (80/20 by volume) [28–30]. The material of the vessel is stainless steel with the crystalline structure of $\gamma$-iron and is implemented with the help of the NXSG4 library [31]. The physics list used is QGSP_BIC_HP. In addition, `/process/eLoss/stepFunction 0.1 0.001` µm and `/process/eLoss/minKinEnergy 10` eV are defined. 120 tubes are placed at a 5 m distance from the sample position, in order to achieve a polar angle coverage of a few degrees.

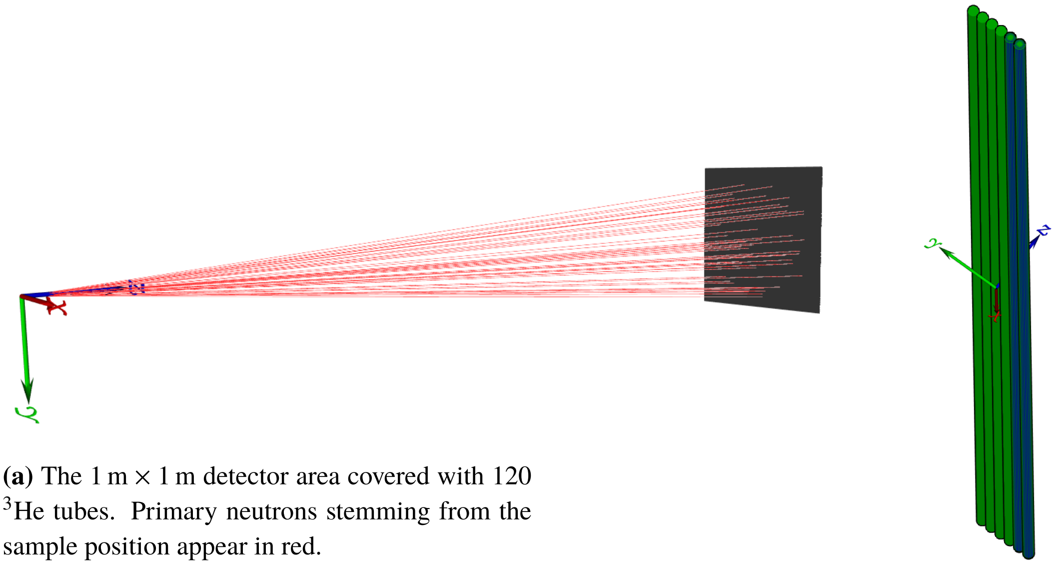

**(a)** The 1 m × 1 m detector area covered with 120 $^3$He tubes. Primary neutrons stemming from the sample position appear in red.

**(b)** Enlarged view of $^3$He tubes. The stainless steel vessel appears in green and the counting gas in blue.

**Figure 3.** The neutron generator is placed at the beginning of the coordinate system, which coincides with the sample position. Simulated neutrons from McStas are emitted towards the 1 m$^2$ geometry at 5 m away along the z-axis. Only neutrons hitting the detector are displayed.

A neutron is counted as incident, when it enters the wall material of a tube. It is counted as detected, when its conversion products have deposited more than 120 keV in the counting gas. The threshold is based on the shape of the experimental pulse height spectrum and has a minor impact on the result of this study. The TOF and wavelength distributions of incident and detected neutrons for instrument configuration 1 are shown in figure 4. For every evaluation that follows the TOF maximum is picked from the respective distribution.

Figure 5a depicts the time-averaged global and local rates for both incident and detected neutrons. The number cited in the legend corresponds to the global time-averaged rate, while the

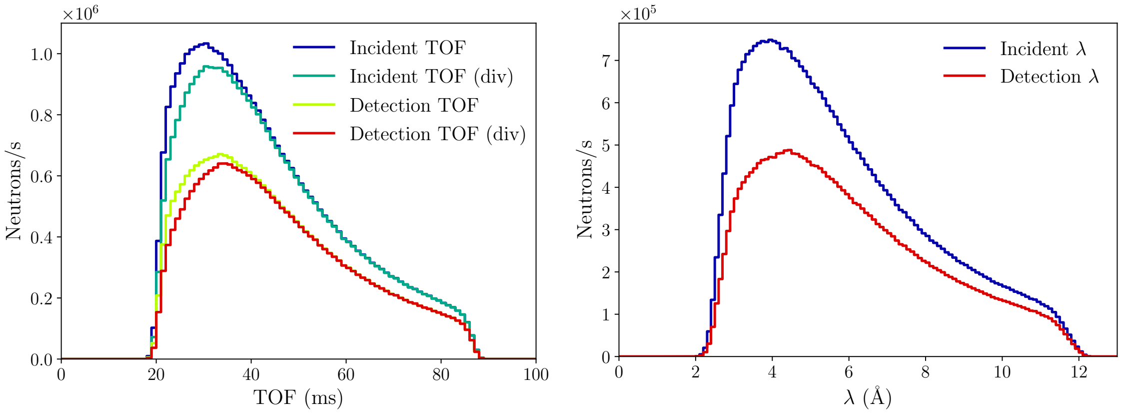

**Figure 4.** Incident and detected neutron TOF distributions for instrument configuration 1, including and excluding divergent neutrons. The TOF maxima can appear at different values for the two cases (left). Incident and detected neutron $\lambda$ distributions for the same instrument configuration (right).

maximum of each histogram corresponds to the local one. In order to extract the peak rates, a 1 ms TOF slice is selected from the respective distribution and only neutrons within this slice are plotted (see figure 5b). The counts are per tube and ms but are converted to Hz when cited in the summary table 2. The inclusion or exclusion of divergent neutrons amounts to a 5% difference only for the first configuration and the particular sample model, and as such it is not presented as a separate case. The same analysis is repeated for all instrument configurations of table 1 and the results are summarised in table 2.

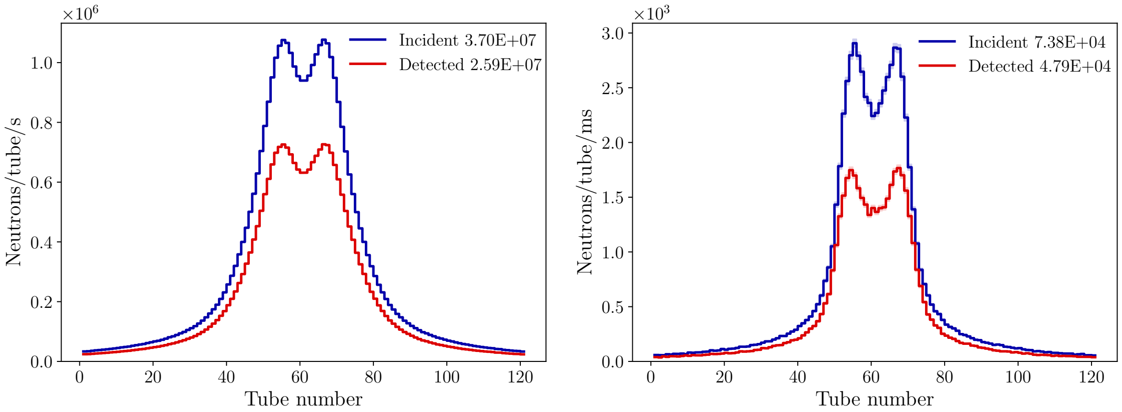

**(a)** Time-averaged rates per $^3$He tube.

**(b)** Peak rates per $^3$He tube.

**Figure 5.** Global (in legend) and local, incident and detection rates for a $^3$He detector and instrument configuration 1.

The operational limit for a non position sensitive $^3$He tube is about 100 kHz [32, 33], dropping at 30–50 kHz for position sensitive tubes. At higher rates the tube performance deteriorates leading to event pile-up. The spatial resolution from charge division is sensitive to the position of the detection

**Table 2.** Summary table with global and local incident and detection rates, both time-averaged and peak ones, for $^3$He tubes.

| config | global average **incident** rate | global average **detection** rate | local average **incident** rate/tube | local average **detection** rate/tube |
|---|---|---|---|---|
| 1 | 37 MHz | 25.9 MHz | 1 MHz | 727 kHz |
| 2 | 7.4 MHz | 5.2 MHz | 225 kHz | 152 kHz |
| 3 | 2.9 MHz | 2 MHz | 91 kHz | 61 kHz |
| config | global peak **incident** rate | global peak **detection** rate | local peak **incident** rate/tube | local peak **detection** rate/tube |
| 1 | 74 MHz | 48 MHz | 2.9 MHz | 1.8 MHz |
| 2 | 15 MHz | 9.6 MHz | 647 kHz | 381 kHz |
| 3 | 6 MHz | 3.9 MHz | 279 kHz | 175 kHz |

event along the tube and is additionally subject to compromise when the operation parameters are favoured towards high rate capability.

The $^3$He technology is clearly inappropriate for the SANS instruments at ESS. Alternative solutions need to be adopted that can serve the scientific case without wasting the intense ESS neutron pulse. A detector option that resembles the $^3$He tube readout but uses a solid $^{10}$B$_4$C converter is explored next.

### 3.2 Rates for the Boron-Coated Straws

A Boron-Coated Straw (BCS) [23, 34] detector is a conventional neutron detector by Proportional Technologies, Inc., which intends to be a cost effective $^3$He replacement technology. A BCS detector consists of an aluminium tube, containing seven copper straws arranged hexagonally (see figure 6b). The tubes are 1 m long with a diameter of 2.54 cm. The straw inner wall is coated with a 1 μm thin B$_4$C converter layer enriched in $^{10}$B by 95%. They are filled with an Ar/CO$_2$ mixture (90/10 by volume) at 0.7 atm. Physics list and `eLoss` parameters are identical to the $^3$He tube simulation (see introduction of section 3.1). The neutron transport in the Al and Cu materials is described with the help of the NCrystal package [35, 36].

A bias voltage is applied between the tube and resistive anode wires, which are tensioned in the center of each straw. This makes the straws work in proportional mode. The charge is read out at both ends of the detector using charge division to acquire the position information. The tubes can be arranged in successive layers in order to achieve the desired coverage, uniformity and detection efficiency.

In the Geant4 model of the current study 5 layers of BCS detectors, referred to as panels, consisting of 40 tubes each cover the same 1 m × 1 m area as the $^3$He detector model. Each tube is rotated by an angle of 10° around its cylindrical axis and the adjacent panels are positioned behind each other with a relative shift of 1.016 cm along the horizontal axis (see figure 6b) for performance optimisation reasons.

A neutron detection event is defined the same way as for the $^3$He tubes, by applying a 120 keV threshold on the energy deposition of the charged conversion products in the counting gas. Due to the complex geometry three different definitions of incident neutrons are used in this section:

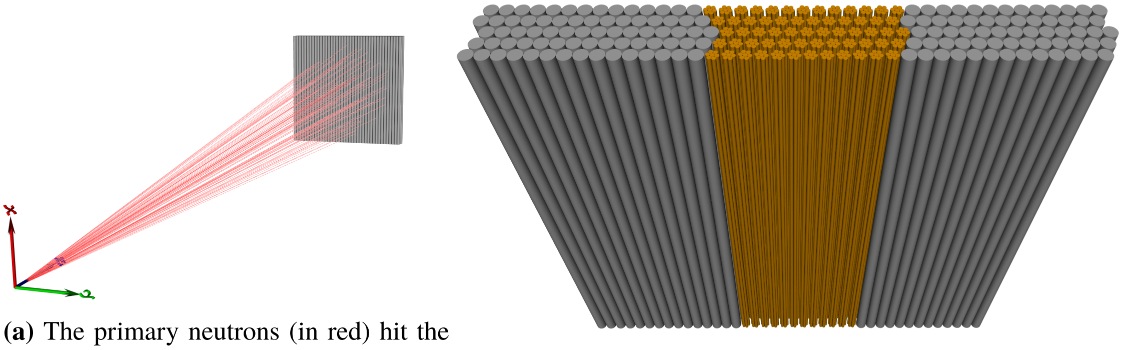

**(a)** The primary neutrons (in red) hit the detectors 5 m away from the sample position.

**(b)** Enlarged view of the 5 overlapping BCS tube panels. Each aluminium tube (grey) contains 7 copper straws (orange) arranged hexagonally.

**Figure 6.** The neutron generator is placed at the beginning of the coordinate system, which coincides with the sample position. Simulated neutrons from McStas are emitted towards 5 panels (×40 tubes/panel) of BCS tubes covering 1 m × 1 m at 5 m away along the z-axis.

incident for the entire detector; incident for a panel; and incident for a straw. A neutron is counted as incident for the entire detector only once, when it enters the wall material of a tube for the first time. On the contrary, a neutron can be counted more than once as incident for a panel but only if it is scattered back from another panel and enters a tube in the panel of interest again. Moreover, a neutron is counted as incident for a straw every time when it enters its copper layer from the outside.

The incident neutron TOF and $\lambda$ spectra per detector panel are depicted in figure 7a and figure 7b. This approach is important for detectors, which provide depth information, as every detector layer is exposed to a different neutron distribution (see figure 8a). From the conversion and detection efficiency of the entire detector for different wavelengths, depicted in figure 8b, it is concluded that the efficiency for lower wavelengths is lower — as expected — and the global detection efficiency is 63% with a detection to conversion ratio of 70%.

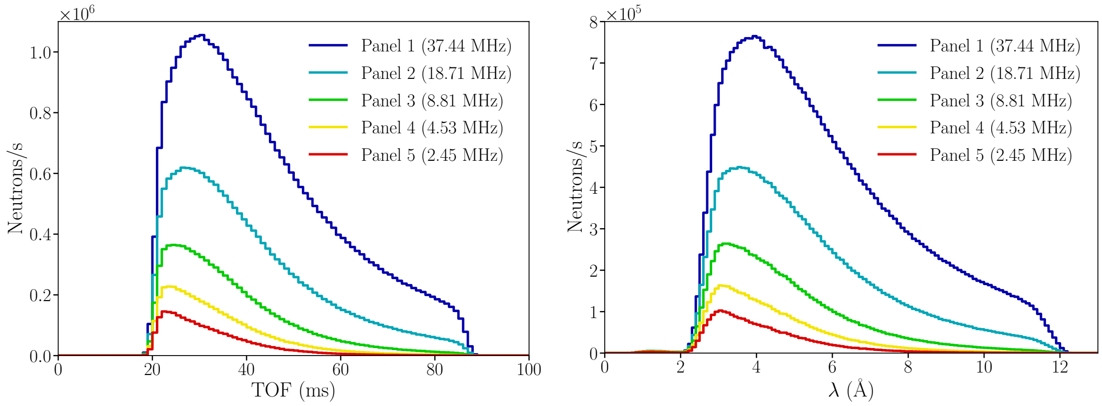

**(a)** **(b)**

**Figure 7.** Incident TOF (a) and $\lambda$ (b) distributions per panel in depth for instrument configuration 1. The respective incident rates appear in the legends.

2018 JINST 13 P07016

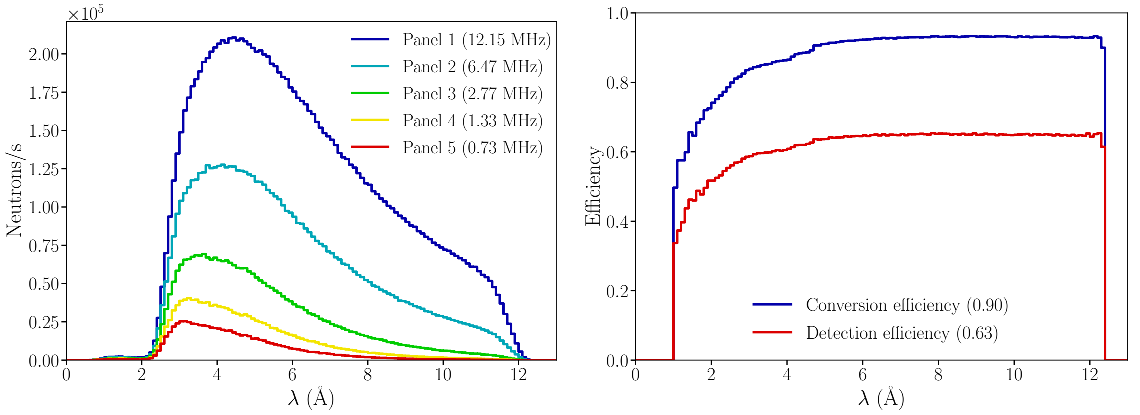

**(a)** **(b)**

**Figure 8.** $\lambda$ distribution of detected neutrons per panel (a). $\lambda$ dependent neutron conversion and detection efficiency for the entire detector (b) for instrument configuration 1. The conversion/detection efficiency is the ratio of the total number of converted/detected neutrons in all straws over the number of incident neutrons for the entire detector for a particular incident $\lambda$. The detection rates per panel and the global average conversion and detection efficiencies appear in the legends.

To get a deeper understanding about the detector system, the detection efficiency of each straw is shown in figure 9. It is defined as the number of detected neutrons in each straw divided by the number of the respective incident neutrons. The efficiency of each straw is represented with a two-dimensional cross-sectional image of the detector geometry similar to figure 6b. The efficiencies of the straws in the first panel indicate that there is a correlation between the scattering angle and the wavelength and it is clear that the straws in the front or with clear sight to the sample have much higher efficiencies than the ones behind them. All straws are identical and so is their detection efficiency for a particular neutron wavelength, so the change of the detection efficiency in depth is the result of the hardening of the neutron spectrum due to the higher absorption cross-section of neutrons with higher wavelength and the thermalisation of the neutrons via scattering. This effect in the spectrum is clearly visible in figure 7.

Figure 10 depicts the time-averaged and peak incident rate for each straw represented the same way as the detection efficiency of the straws. The peak rates are extracted the same way as for the $^3$He tubes, by counting neutrons only from a selected 1 ms TOF slice that results in the highest instantaneous rates. The tubes with the highest peak incident rates are localised in the center of

2018 JINST 13 P07016

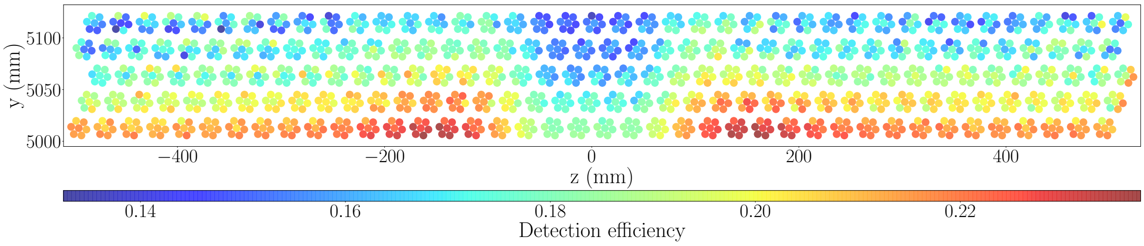

**Figure 9.** Detection efficiency per straw for instrument configuration 1.

the panels because the highest incident rates occur when the relatively high energy neutrons are scattered on the sample in small angles and most of them enter the same straws. Figure 10 gives an enlarged view of these straws and also shows the peak detected rates of the straws with the highest values. The highest peak rates appear in the straws of the first panel for all three configurations. A summary of the estimated incident and detection rates can be found in table 3.

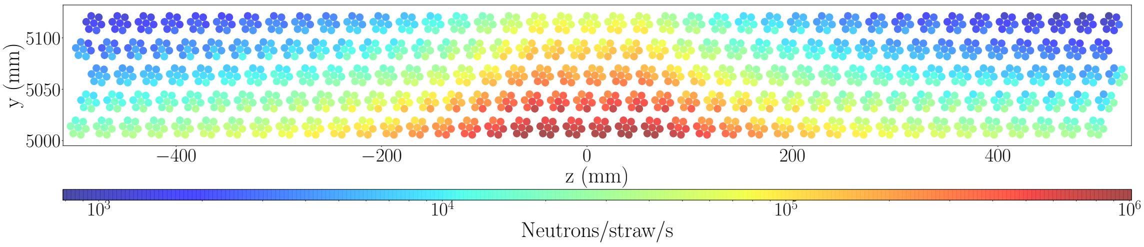

**(a)** Time-averaged incident rate for per BCS straw.

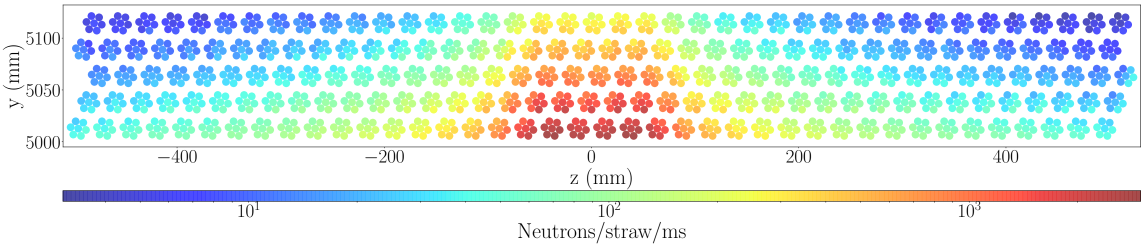

**(b)** Peak incident rate per BCS straw.

**Figure 10.** Time-averaged and peak incident rate per BCS straw for instrument configuration 1.

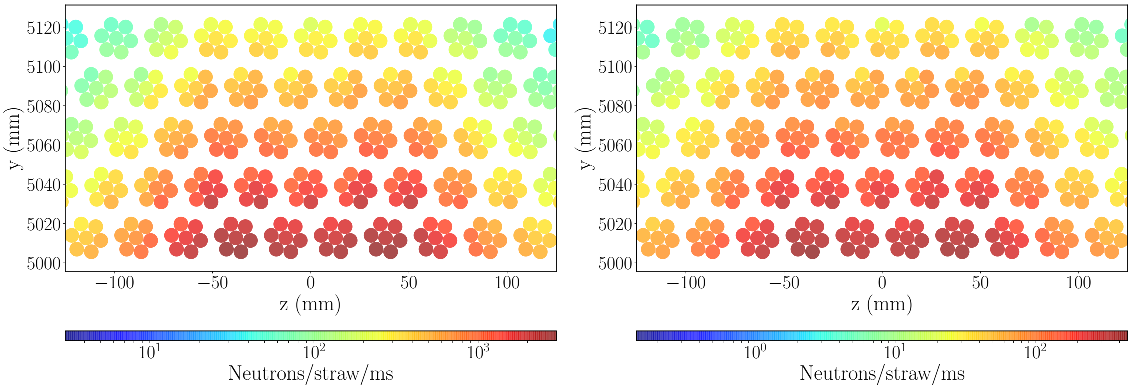

**(a)** **(b)**

**Figure 11.** Peak incident (a) and detection (b) rates for the central straws for instrument configuration 1.

Similarly to the $^3$He tubes, the BCS straws are expected to start saturating at 50–100 kHz. For instrument configuration 1 with the shortest instrument collimation, peak rates as high as 458 kHz for a single straw are derived. This implies that the operation of such a detector is subject to the same limitations as a $^3$He tube.

**Table 3.** Summary table with global and local incident and detection rates, both time-averaged and peak ones, for the BCS detector.

| config | global average **incident** rate | global average **detection** rate | local average **incident** rate/straw | local average **detection** rate/straw |
|---|---|---|---|---|
| 1 | 37.3 MHz | 23.5 MHz | 1.01 MHz | 187 kHz |
| 2 | 7.48 MHz | 4.70 MHz | 211 kHz | 39.0 kHz |
| 3 | 2.91 MHz | 1.82 MHz | 86.3 kHz | 15.0 kHz |
| config | global peak **incident** rate | global peak **detection** rate | local peak **incident** rate/straw | local peak **detection** rate/straw |
| 1 | 74.3 MHz | 64.2 MHz | 2.99 MHz | 458 kHz |
| 2 | 15.1 MHz | 13.1 MHz | 651 kHz | 100 kHz |
| 3 | 6.11 MHz | 5.29 MHz | 283 kHz | 47.0 kHz |

## 4 Tackling the ESS flux with pixel geometries

The limitations the tube detector geometries are subject to for the ESS SANS rates can be alleviated with the use of detectors whose anodes consist of 2D pixels with individual readout, which leads to a more efficient distribution of the incoming neutron flux. The pixels may vary in shape to accommodate an even spread of detection events, satisfy spatial resolution requirements, as well as to geometrically facilitate the polar angle coverage.

In the following sections two different implementations of 2D pixels are presented, a detector with square pixels (Solid state Neutron Detector (SoNDe)) and one with trapezoidal pixels (Boron Array Neutron Detector (BAND-GEM)). These detectors are developed in the context of SANS for ESS and are the baseline choices for the respective instruments. As these detector technologies are high rate capable, only the incident rates are considered in the following evaluation.

### 4.1 Rates for the SoNDe detector

The first approach for handling the SANS rates with 2D anode pixels is the SoNDe detector [37–40], adopted by the SKADI instrument. The detector surface area is covered by multiple scintillator tiles of $^6$Li-glass (GS20® [41]) with the respective Multi-anode PMT (MaPMT) placed right behind them. Each tile is 48.5 mm × 48.5 cm in size for the chosen MaPMT model (H12700 [42]) and is served by 64 (8 × 8) MaPMT pixels. The detector consists of 400 modules in total, which will be equipping three different detector banks, as shown in figure 1. For the sake of the rate evaluation though, all 400 modules are assumed to be occupying the rear detector in an arrangement of 1 m × 1 m (20 × 20 modules) placed 5 m after the sample (see figure 12).

An incident neutron is counted the first time it enters the scintillator glass. The physics taking place inside the scintillator material and beyond is not included in the Geant4 simulation. Figures 13 and 14 respectively depict the incident time-averaged and peak rates per SoNDe module and pixel.

The total number of pixels for the current Geant4 implementation of SoNDe is 25600. The SANS technique results in widespread rates over a large number of pixels, contrary to other neutron techniques. It does not trigger highly localised detection events in time and space. Thus, it is

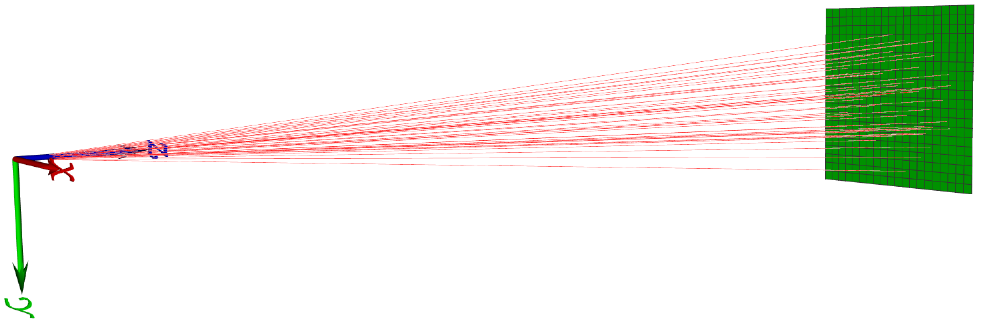

**Figure 12.** Geometry of the SoNDe scintillator tiles in an arrangement of 400 (20 × 20) modules occupying a 1 m × 1 m rear detector bank. In red appear primary neutrons originating from the sample.

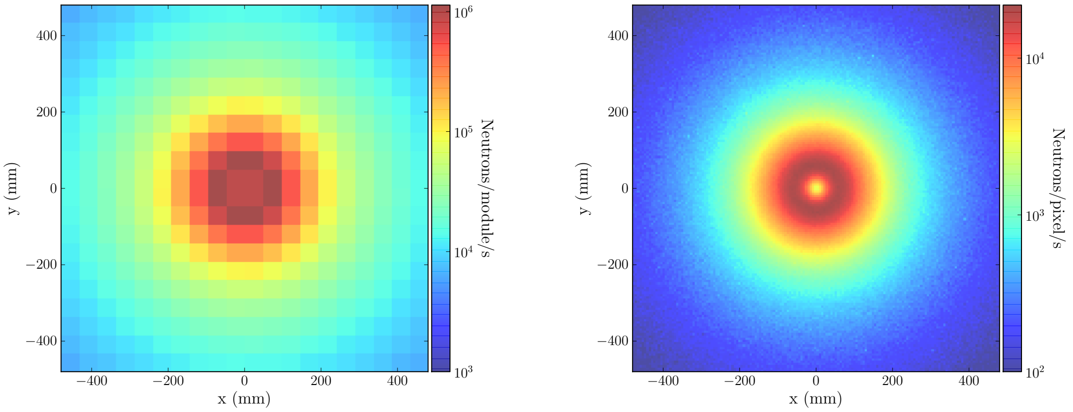

**(a)** **(b)**

**Figure 13.** Time-averaged incident rates per SoNDe module (a) or pixel (b) for instrument configuration 1.

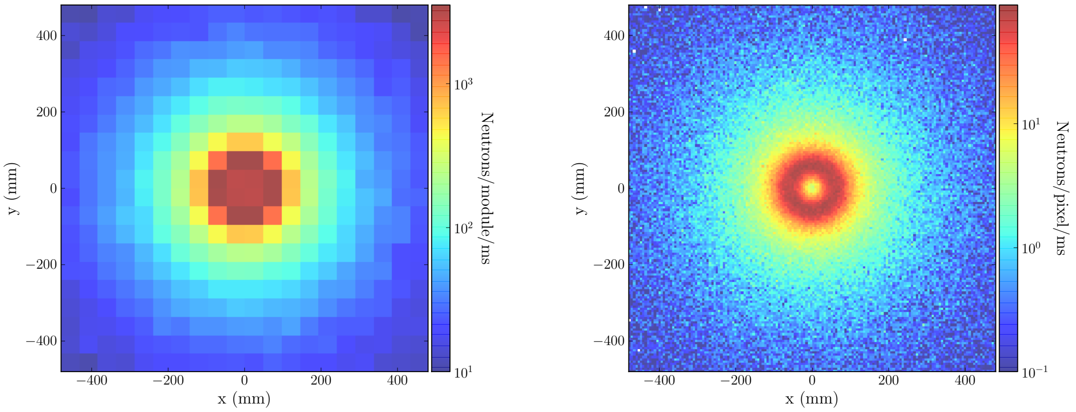

**(a)** **(b)**

**Figure 14.** Peak incident rates per SoNDe module (a) or pixel (b) for instrument configuration 1.

**Table 4.** Summary table with incident time-averaged and peak rates for the SoNDe detector.

| config | global average incident rate | local average incident rate/module | local average incident rate/pixel |
|---|---|---|---|
| 1 | 37 MHz | 1.1 MHz | 21.8 kHz |
| 2 | 5.1 MHz | 167 kHz | 3.6 kHz |
| 3 | 2.9 MHz | 99 kHz | 2.3 kHz |
| config | global peak incident rate | local peak incident rate/module | local peak incident rate/pixel |
| 1 | 73 MHz | 3.5 MHz | 90 kHz |
| 2 | 10 MHz | 550 kHz | 21 kHz |
| 3 | 6 MHz | 341 kHz | 14 kHz |

imperative for the design of the data acquisition chain to take into account all aspects of the rate distribution, and to ensure all buffers are adequate for the expected data patterns.

It is interesting to look at what these values mean in terms of data throughput. For the highest flux collimation of the instrument, the global peak incident rate is about 73 MHz. This means that in the hottest millisecond of the pulse, 73000 neutrons will enter the detector. Assuming that every neutron triggers a signal over threshold on 1–3 pixels, a 64 bit time-stamp assigned to every fired pixel and an 8–15 bit pixel ID assigned to pixel location, the total amount of data the detector pushes out through the optical fibers per second can be calculated as:

$$\text{Data rate (bps)} = n_{\text{pixels/neutron}} \times n_{\text{peak neutrons/s}} \times \left(\text{timestamp} + \text{pixelID}\right) \text{ bits/pixel} \tag{4.1}$$

and is in the range of 5–17 Gb/s for a 100% efficient detector.

The rate values of table 4 demonstrate the need for operating this detector in pixel mode and not in Anger camera mode, as the shipping of the ADC values required by the algorithm would make the data rates forbidding for the DAQ. Detectors are foreseen to run in different operation modes, e.g. calibration, diagnostics, standard. In non-standard operation it is anticipated that the data rate can significantly increase because of the additional information collected. However, it is common to tolerate pile-ups in this context, as the DAQ under such circumstances usually serves a different purpose and event rejection can be applied.

### 4.2 Rates for the BAND-GEM detector

The second detector example of an anode pixel implementation is the Boron Array Neutron Detector (BAND-GEM) [43–47]. It is a trapezoidal GEM module with an intricate cathode design, which consists of consecutive lamellae forming a Venetian blind (see figure 15). In order to achieve the polar and azimuthal angle coverage for the rear detector of a SANS instrument, several trapezoidal BAND-GEM modules are assembled together to create a polygonal cross section as in figure 15a.

The anode on which the electrical signal is induced is divided in equal slices of 10° in the azimuthal ($\phi$) direction and bands with a constant pitch of 4 mm in the polar angle ($\theta$) direction (see figure 16). The shape introduced for this study does not perfectly match the engineering drawing of the actual demonstrator but the simplification serves the purpose of the rate analysis without a

2018 JINST 13 P07016

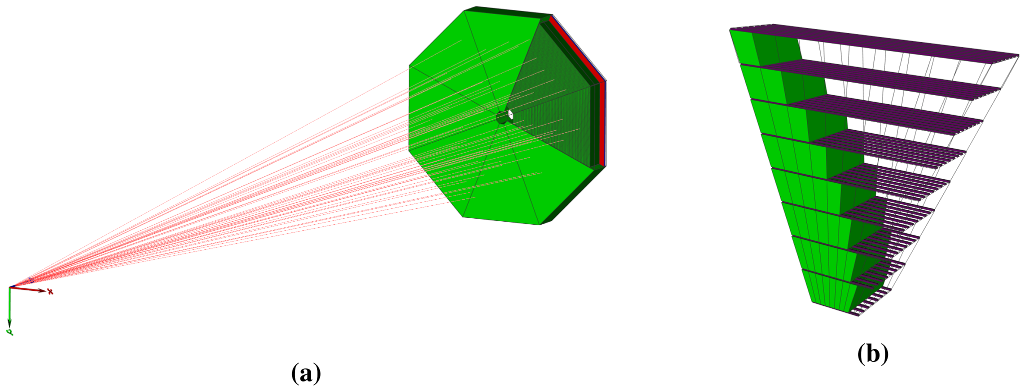

**Figure 15.** Rear detector bank composed of eight BAND-GEM modules arranged in a polygon (a). The anode panels are placed on the back of the detector (red). The open space in the middle is reserved for the installation of a transmission monitor. The cathode structure (purple) of a single segment with gas volumes (green) in between (b). The latter geometry shows a reduced number of cathodes to allow for better visualisation.

significant compromise. Practically, the pixels can be further subdivided in the azimuthal direction at the outer polar angles to locally increase the spatial resolution or merged at very low angles, where their size is below the required spatial resolution to reduce their number.

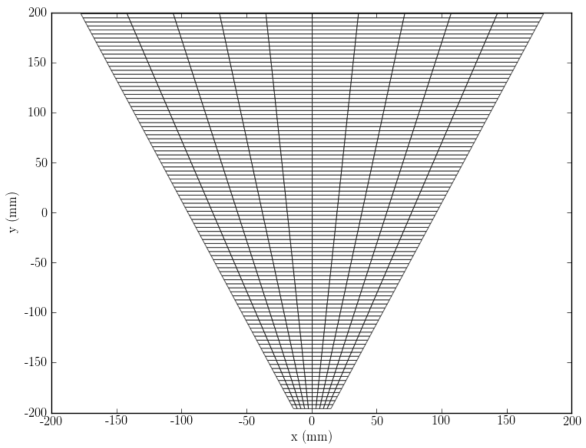

**Figure 16.** Anode pad geometry for a BAND-GEM module. In the particular implementation there are 98 rows of pixels with 10 pixels in each row.

Following the same analysis steps as with the previous detectors, the derived incident rate estimates are summarised in table 5. Figure 17 demonstrates the time-averaged and peak incident rates for instrument configuration 1. The BAND-GEM technology has been proven to successfully handle thermal neutron rates of up to 40 MHz/cm$^2$ [43], which renders it an appropriate choice for the ESS SANS instruments in terms of rate capability.

A single BAND-GEM module contains 980 pixels in the current Geant4 implementation. For the full detector of eight segments, the total number of channels is 7840. Using eq. 4.1 with the assumption of 1–3 triggered pixels/neutron, 8–15 bits for the pixel ID representation and 100% detection efficiency the data throughput that 8 segments would push out is approximately 5–16 Gb/s.

2018 JINST 13 P07016

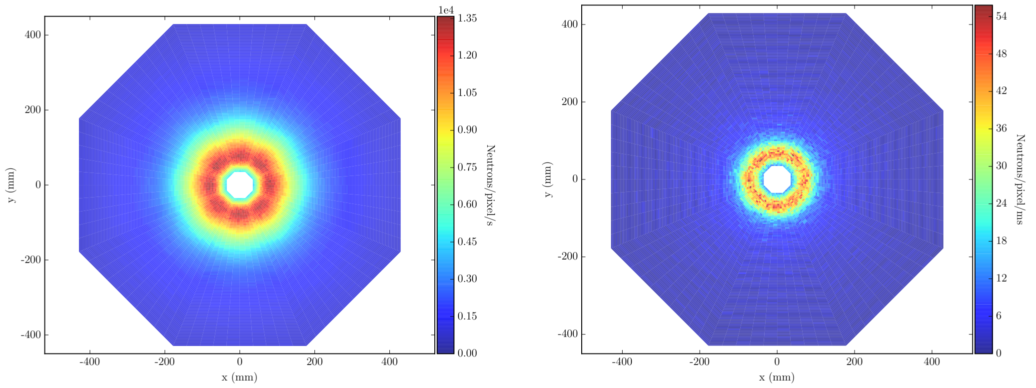

**(a)** **(b)**

**Figure 17.** Time-averaged (a) and peak (b) incident rates for the BAND-GEM detector and instrument configuration 1.

**Table 5.** Summary table with incident time-averaged and peak rates for the BAND-GEM detector.

| config | global average incident rate | local average incident rate/pixel | global peak incident rate | local peak incident rate/pixel |
|---|---|---|---|---|
| 1 | 34 MHz | 13.6 kHz | 68 MHz | 55.9 kHz |
| 2 | 7 MHz | 3.1 kHz | 14 MHz | 18.1 kHz |
| 3 | 2.7 MHz | 1.4 kHz | 5.7 MHz | 12.7 kHz |

## 5 Rates for the transmission detector

Aside from the rate capability of the SCS, the transmission detectors installed at the ESS SANS instruments need special attention. They are exposed to a large fraction of the direct beam and the increased neutron flux offers the possibility for per pulse normalisation. The new operation environment raises several questions regarding the required spatial resolution, detection efficiency, stability and longevity of such a detector.

To this end, a square geometry of 6 cm × 6 cm segmented in 1 cm × 1 cm size pixels is placed 5 m away from the sample covering polar angles up to 0.4°. The simulated data input uses the same sample model as before, only this time the transmitted neutrons which do not interact with the sample are also propagated until the transmission monitor. The total number of incident neutrons which enter the detector's active volume are counted and summarised in the form of global time-averaged and peak rates in table 6 for all instrument configurations.

**Table 6.** Summary table with global time-averaged and peak incident rates for a 6 cm × 6 cm transmission detector.

| config | global average incident rate | global peak incident rate |
|---|---|---|
| 1 | 911 MHz | 3.6 GHz |
| 2 | 193 MHz | 785 MHz |
| 3 | 78 MHz | 219 MHz |

A non-exhaustive list of implementations is evaluated below; a generic pixelated anode with a 1 cm × 1 cm pixel size, a SoNDe-like implementation based on the H9500 MaPMT model [48] with a 3 mm × 3 mm pixel size, a wire gas counter of 15 wires at a 4 mm pitch and an ionisation chamber operated in current mode. The respective local time-averaged and peak incident rates are presented in figure 18 and table 7.

**Table 7.** Summary table with incident time-averaged and peak rates for various implementations of the transmission detector for all instrument configurations.

| config | local average incident rate $/\mathrm{cm}^2$ /9 $\mathrm{mm}^2$ /wire | local peak incident rate $/\mathrm{cm}^2$ /9 $\mathrm{mm}^2$ /wire |
|---|---|---|
| 1 | 52 / 5 / 95 MHz | 206 / 22 / 385 MHz |
| 2 | 30 / 4 / 37 MHz | 134 / 19 / 154 MHz |
| 3 | 17 / 3 / 20 MHz | 49 / 11 / 81 MHz |

For a 1 $\mathrm{cm}^2$ pixel anode, a peak incident rate of 200 $\mathrm{MHz/cm}^2$ translates to an average pulse spacing of 5 ns and a typical detector rise time of 500 ps, rendering a full efficiency implementation impossible. Assuming a 1% detection efficiency, the peak detection rate drops to 2 $\mathrm{MHz/cm}^2$. A fast detector with a single converter layer, e.g. a GEM, could satisfy this requirement and possibly allow for a higher detection efficiency up to 15–20% before it saturates. The analysis above also demonstrates that the 1 $\mathrm{cm}^2$ pixel size is the upper limit for use in a high flux environment.

A SoNDe-like implementation with a smaller square pixel size of 3 mm × 3 mm, equipped with a fast scintillator like the GS20 glass is thus another possibility. The upper incident limit estimated here is at 22 MHz/pixel and given the detector has a high efficiency (>75% [39]), either the incoming neutron flux has to be significantly attenuated or the detection efficiency has to be reduced for the module to operate.

A wire gas counter without position information, covering the same active area, e.g. with 15 wires at 4 mm pitch, is explored next. With an incident peak rate of 385 MHz/wire (see table 7) and a detection efficiency of $10^{-4}$ (e.g. with $N_2$ as counting gas), the order of magnitude for the peak detection rate is still around 40 kHz/wire, which poses a challenge for the stability of such a detector.

Last but not least, a $^3$He- or $^{10}$B-based ionisation chamber can be considered, if only integrated flux is required from a transmission detector. Both gas and solid state implementations are used in high flux environments for reactor or beam monitoring. They are operated in current mode, i.e. the collected charge is integrated in time. The current is proportional to the direct ionisation charge released in the active volume, as the chamber is operated with no gain. This type of detectors have demonstrated operation stability and can perform over a large dynamic range. However, as they are uncommon in the neutron scattering field, development is needed to customise them for the particular use. Similar development steps would be necessary for other more exotic detector solutions, in order to ensure their performance suitability and stability [49–51].

As the transmission detector is exposed to a large fraction of the direct beam, the outgoing data rates could prove challenging. Indeed, with the assumptions of a 20% detection efficiency, 1–2 pixels triggered per event, a 64 bit time-stamp per pixel and an 8–10 bit pixel ID, the output data rate is 53–107 Gbps for instrument configuration 1. To stay below the 100 Gbps limit of the optical

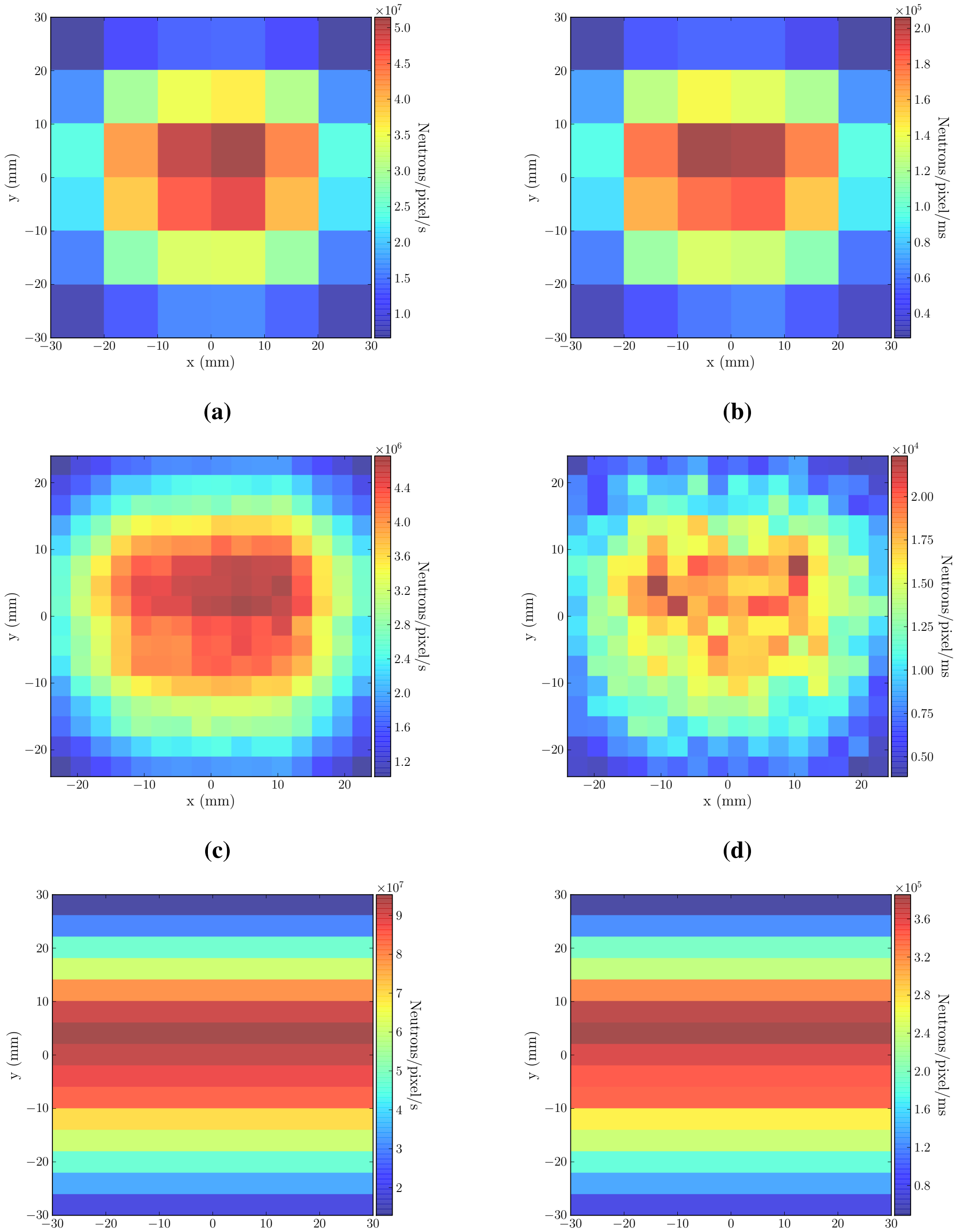

**(a)** **(b)**

**(c)** **(d)**

**(e)** **(f)**

**Figure 18.** Incident time-averaged (left) and peak (right) rates for a transmission detector of a 1 cm × 1 cm pixel size (a, b), a 3 mm × 3 mm pixel size (c, d) and a wire gas counter (e, f) for instrument configuration 1.

fiber, the output data rate can be lowered by further reducing the detector efficiency, the accuracy of the time stamp or by optimising the data format to contain a single time stamp per event for all triggered pixels. A detailed analysis of the instrument requirements with respect to the detector ones can set the limits of the design parameters.

## 6 Conclusions

As the ESS source will subject the detectors to unprecedented neutron fluxes, it is scientifically imperative that the new detector requirements are fulfilled. One of the bigger challenges is the rate capability of detectors used in SANS techniques, whilst satisfying other requirements. An overview of the incident and detection rate estimates anticipated for the upcoming SANS instruments at ESS is presented. The rate capabilities of various detector technologies are discussed for the rear SCS, as well as for the transmission detector. Lower and upper limits are respectively set, as only the coherent signal from the sample is used. The time-averaged SCS rates need to be corrected upwards by a few % to include the incoherent component, while the same correction has to be applied downwards for the transmission rates. A more detailed look at the time dependence of the incoherent signal would be necessary to adjust the peak rate values. The study is based on a baseline LoKI instrument model. SKADI is foreseen to operate with longer collimation lengths compared to LoKI, which immediately relaxes the detection rate requirements.

It becomes apparent that tube detectors can potentially compromise the instrument performance for high flux configurations. A standard $^3$He tube would saturate already at 100–200 kW source power. A BCS straw is expected to saturate at 800–1000 kW source power. The tube parameters can be adjusted, so as to distribute the detection events over multiple layers but such an improvement cannot adequately lift the saturation limit of this detector type. Moreover, the addition of multiple detection layers enhances the scattering effects with a negative impact on the spatial resolution of the detector. A custom readout electronics design can partially alleviate the saturation but again at the cost of spatial resolution. Last, both tube technologies explored in this study employ a closed gas system, which prevents counting gas purification and impurity filtering, and has consequences on the quality of operation with sustained high rates over the years. Particularly for BCS, long term operation under such conditions has not been demonstrated.

Alternative technologies, like SoNDe and BAND-GEM, with 2D anode pixels are a more suitable choice to exploit the full ESS source power. The pixel size and shape can be designed for optimal spatial resolution and rate capability. In the SoNDe case the rate estimates indicate that the detector needs to be operated in pixelated mode, as the Anger camera mode would result in data rates too excessive for an affordable DAQ system. In the BAND-GEM case the open gas system allows for efficient monitoring of the gas quality and composition, which contributes to the stability and longevity of the detector. As the amount of channels and data output dramatically increase, special consideration is needed for the choice of bandwidths and buffers throughout the DAQ chain.

Last but not least a first glance at the rates for the transmission monitor is attempted. Few different technologies are discussed in this context. An important conclusion is that for a position sensitive detector, the pixel size cannot exceed the 1 cm$^2$ for saturation reasons. Moreover, it turns out that the output data rate can be more demanding for this detector than for the SCS. An understanding of the spatial resolution, efficiency and accuracy requirements from the instrument side is vital for the customisation of the proposed technologies, as well as the design of the DAQ chain.

## Acknowledgments

Richard Hall-Wilton, Kalliopi Kanaki and Thomas Kittelmann would like to acknowledge support from the EU Horizon2020 BrightnESS grant (676548). Richard Hall-Wilton and Kalliopi Kanaki would also like to acknowledge support from the EU Horizon2020 SoNDe grant (654124). Milán Klausz would like to acknowledge the supervision of Péter Zagyvai. Computing resources were provided by the DMSC Computing Centre (https://europeanspallationsource.se/data-management-software/computing-centre). The authors would like to thank Richard Heenan for his valuable comments on the manuscript. Kalliopi Kanaki would like to thank Ramsey Al Jebali, Morten Jagd Christensen and Jonas Nilsson for the useful conversations and support with python.

## References

[1] S. Peggs et al., *ESS Conceptual Design Report*, ESS 2012-001, https://europeanspallationsource.se/sites/default/files/downloads/2017/09/CDR_final_120206.pdf.

[2] S. Peggs et al., *ESS Technical Design Report*, ESS 2013-001, https://europeanspallationsource.se/sites/default/files/downloads/2017/09/TDR_online_ver_all.pdf.

[3] O. Kirstein et al., *Neutron Position Sensitive Detectors for the ESS*, `PoS(Vertex2014)029`.

[4] A.J. Jackson et al., *LoKI — A Broad Band High Flux SANS Instrument for the ESS*, in *Proceedings of ICANS XXI*, Mito, Ibaraki, Japan, October 2015, pp. 263–272.

[5] A. J. Jackson and K. Kanaki, *LoKI - A broad-band SANS instrument*, https://europeanspallationsource.se/sites/default/files/files/document/2017-09/loki_proposal_stc_sept2013.pdf, 2012.

[6] S. Jaksch et al., *Concept for a Time-of-Flight Small Angle Neutron Scattering Instrument at the European Spallation Source*, *Nucl. Instrum. Meth.* **A 762** (2014) 22 [`arXiv:1403.2534`].

[7] S. Jaksch, *Considerations about Chopper Configuration at a time-of-flight SANS Instrument at a Spallation Source*, *Nucl. Instrum. Meth.* **A 835** (2016) 61 [`arXiv:1606.04206`].

[8] L.A. Feigin and D. Svergun, *Structure Analysis by Small-Angle X-Ray and Neutron Scattering*, Springer (1987).

[9] B.T.M. Willis and C.J. Carlile, *Experimental Neutron Scattering*, Oxford University Press (2009).

[10] I. Stefanescu et al., *Neutron detectors for the ESS diffractometers*, 2017 *JINST* **12** P01019 [`arXiv:1607.02324`].

[11] K. Lefmann and K. Nielsen, *McStas, a general software package for neutron ray-tracing simulations*, *Neutron News* **10** (1999) 20.

[12] P. Willendrup, E. Farhi and K. Lefmann, *McStas 1.7 - a new version of the flexible monte carlo neutron scattering package*, *Physica* **B 350** (2004) E735.

[13] K.H. Andersen, M. Bertelsen, L. Zanini, E.B. Klinkby, T. Schönfeldt, P.M. Bentley et al., *Optimization of moderators and beam extraction at the ESS*, *J. Appl. Cryst.* **51** (2018) 264.

[14] GEANT4 collaboration, S. Agostinelli et al., *GEANT4: A Simulation toolkit*, *Nucl. Instrum. Meth.* **A 506** (2003) 250.

[15] J. Allison et al., *Geant4 developments and applications*, *IEEE Trans. Nucl. Sci.* **53** (2006) 270.

[16] J. Allison et al., *Recent developments in Geant4*, *Nucl. Instrum. Meth.* **A 835** (2016) 186.

[17] T. Kittelmann, I. Stefanescu, K. Kanaki, M. Boin, R. Hall-Wilton and K. Zeitelhack, *Geant4 based simulations for novel neutron detector development*, *J. Phys. Conf. Ser.* **513** (2014) 022017 [`arXiv:1311.1009`].

[18] T. Kittelmann, E. Klinkby, E. Knudsen, P. Willendrup, X. Cai and K. Kanaki, *Monte Carlo Particle Lists: MCPL*, *Comput. Phys. Commun.* **218** (2017) 17.

[19] *MCPL documentation and GitHub repository*, https://mctools.github.io/mcpl/ (accessed July 2018).

[20] E. Dian, K. Kanaki, G. Ehlers, R.J. Hall-Wilton, A. Khaplanov, T. Kittelmann et al., *Scattered neutron background in thermal neutron detectors*, *Nucl. Instrum. Meth.* **A 902** (2018) 173 [`arXiv:1801.05686`].

[21] F. Piscitelli et al., *The Multi-Blade Boron-10-based Neutron Detector for high intensity Neutron Reflectometry at ESS*, 2017 *JINST* **12** P03013 [`arXiv:1701.07623`].

[22] M. Anastasopoulos et al., *Multi-Grid Detector for Neutron Spectroscopy: Results Obtained on Time-of-Flight Spectrometer CNCS*, 2017 *JINST* **12** P04030 [`arXiv:1703.03626`].

[23] J.L. Lacy, A. Athanasiades, C.S. Martin, L. Sun and G.L. Vazquez-Flores, *The evolution of neutron straw detector applications in homeland security*, *IEEE Trans. Nucl. Sci.* **60** (2013) 1140.

[24] S. Mühlbauer et al., *The new small-angle neutron scattering instrument SANS-1 at MLZ-characterization and first results*, *Nucl. Instrum. Meth.* **A 832** (2016) 297.

[25] R.K. Heenan et al., *SANS2D at the ISIS Second Target Station*, in *Proceedings of ICANS-XVII*, Santa Fe, New Mexico, U.S.A., 25–29 April 2005, pp. 780–785.

[26] J.K. Zhao, C.Y. Gao and D. Liu, *The extendedQ-range small-angle neutron scattering diffractometer at the SNS*, *J. Appl. Cryst.* **43** (2010) 1068.

[27] C. D. Dewhurst et al., *The small-angle neutron scattering instrument D33 at the Institut Laue-Langevin*, *J. Appl. Cryst.* **49** (2016) 1.

[28] GE Digital Solutions, https://www.gemeasurement.com/radiation-measurement/neutron-scattering/helium-3-position-sensitive-neutron-detector (accessed July 2018).

[29] Toshiba Electron Tubes and Devices, https://etd.canon/eng/product/prden.php?type=cat&search=500000300000 (accessed July 2018).

[30] R.A. Campbell, H.P. Wacklin, I. Sutton, R. Cubitt and G. Fragneto, *Erratum to: FIGARO: The new horizontal neutron reflectometer at the ILL*, *Eur. Phys. J. Plus* **130** (2015) 107.

[31] T. Kittelmann and M. Boin, *Polycrystalline neutron scattering for Geant4: NXSG4*, *Comput. Phys. Commun.* **189** (2015) 114.

[32] G. Knoll, *Radiation Detection and Measurement*, 4th ed., John Wiley & Sons, Inc., U.S.A. (2010) ch. 14, pp. 535–536, 539.

[33] ILL Neutron Data Booklet, https://www.ill.eu/fileadmin/user_upload/ILL/1_About_ILL/Documentation/NeutronDataBooklet.pdf, 2nd Edition, July 2003, ch. 3.3.8 (accessed July 2018).

[34] J.L. Lacy et al., *Boron-coated straw detectors: A novel approach for helium-3 neutron detector replacement, in IEEE Nuclear Science Symposium and Medical Imaging Conference* (2010) 3971, doi:10.1109/NSSMIC.2010.5874561.

[35] X.X. Cai and T. Kittelmann, *NCrystal: a library for thermal neutron transport in crystals*, https://mctools.github.io/ncrystal/ (accessed July 2018)

[36] K. Kanaki, T. Kittelmann, X.X. Cai, E. Klinkby, E. B. Knudsen, P. Willendrup et al., *Simulation tools for detector and instrument design*, *Physica* **B** (2018) in press.

[37] S. Jaksch et al., *Recent Developments SoNDe High-Flux Detector Project*, in *Proceedings of International Conference on Neutron Optics (NOP2017)*, 2017, in press.

[38] *Scintillation detector with a high count rate*, Patent PCT/EP2015/074 200 (2015).

[39] S. Jaksch, R. Engels, G. Kemmerling, C. Gheorghe, P. Pahlsson, S. Désert et al., *Cumulative Reports of the SoNDe Project July 2017*, `arXiv:1707.08679`.

[40] The SoNDe project at FZJ, http://www.fz-juelich.de/jcns/jcns-2/EN/Forschung/Instruments-for-ESS/SoNDe-Projekt/_node.html (accessed July 2018).

[41] GS20 $^{6}$Li-glass specifications, https://scintacor.com/products/6-lithium-glass (accessed July 2018).

[42] MaPMT H12700 specifications by Hamamatsu Photonics, https://www.hamamatsu.com/resources/pdf/etd/H12700_TPMH1348E.pdf (accessed July 2018).

[43] G. Croci, G. Albani, C. Cazzaniga, E. P. Cippo, E. Schooneveld, G. Claps et al., *Diffraction measurements with a boron-based GEM neutron detector*, *Europhys. Lett.* **107** (2014) 12001.

[44] E. Perelli Cippo et al., *A GEM-based thermal neutron detector for high counting rate applications*, 2015 *JINST* **10** P10003.

[45] G. Albani, E. Perelli Cippo, G. Croci, A. Muraro, E. Schooneveld, A. Scherillo et al., *Evolution in boron-based GEM detectors for diffraction measurements: from planar to 3D converters*, *Meas. Sci. Technol.* **27** (2016) 115902.

[46] A. Muraro, G. Croci, E. Perelli Cippo, G. Grosso, C. Höglund, G. Albani et al., *Performance of the high-efficiency thermal neutron BAND-GEM detector*, *Prog. Theor. Exp. Phys.* **2018** (2018) 023H01.

[47] G. Albani, *High rate thermal neutron gaseous detector for use at neutron spallation sources*, Ph.D. Thesis, Dipartimento di Fisica "G. Occhialini", Università degli Studi di Milano-Bicocca (2017).

[48] MaPMT H9500 specifications by Hamamatsu Photonics, https://www.hamamatsu.com/resources/pdf/etd/H9500_H9500-03_TPMH1309E.pdf (accessed July 2018).

[49] F.D. Amaro, C.M.B. Monteiro, J.M.F. dos Santos and A. Antognini, *Novel concept for neutron detection: proportional counter filled with* $^{10}$*B nanoparticle aerosol*, *Sci. Rep.* **7** (2017) 41699 [*Erratum ibid.* **8** (2018) 46942].

[50] M. Cortesi, R. Zboray, A. Kaestner and H.-M. Prasser, *Development of a cold-neutron imaging detector based on thick gaseous electron multiplier*, *Rev. Sci. Instrum.* **84** (2013) 023305.

[51] K.A. Nelson, N.S. Edwards, N.J. Hinson, C.D. Wayant and D.S. McGregor, *A suspended boron foil multi-wire proportional counter neutron detector*, *Nucl. Instrum. Meth.* **A 767** (2014) 14.